Technical Note

Title: Finite element analysis predicts experimental failure patterns in vertebral bodies loaded via intervertebral discs up to large deformation

Authors:

Allison L. Clouthier[a, 1]

email: allison.clouthier@queensu.ca

Hadi S. Hosseini[a]

email: hadi.seyed@istb.unibe.ch

Ghislain Maquer[a]

email: ghislain.maquer@istb.unibe.ch

Philippe K. Zysset[a]

email: philippe.zysset@istb.unibe.ch

a. Institute for Surgical Technology and Biomechanics, University of Bern Stauffacherstrasse 78, 3014 Bern, Switzerland

1. Present Address: Department of Mechanical and Materials Engineering, Queen's University, 130 Stuart St., Kingston, ON, Canada.

Corresponding Author:

Philippe K. Zysset
Institute for Surgical Technology and Biomechanics, University of Bern
Stauffacherstrasse 78
3014 Bern, Switzerland
Tel: +41 31 631 59 25
Email: philippe.zysset@istb.unibe.ch

Disclosure Statement: The authors have no affiliations from which financial or other benefits may arise to disclose.

Word Count: 2796

Finite element analysis predicts experimental failure patterns in vertebral bodies loaded via intervertebral discs up to large deformation

Vertebral compression fractures are becoming increasingly common. Patient-specific nonlinear finite element (FE) models have shown promise in predicting yield strength and damage pattern but have not been experimentally validated for clinically relevant vertebral fractures, which involve loading through intervertebral discs with varying degrees of degeneration up to large compressive strains. Therefore, stepwise axial compression was applied *in vitro* on segments and performed *in silico* on their FE equivalents using a nonlocal damage-plastic model including densification at large compression for bone and a time-independent hyperelastic model for the disc. The ability of the nonlinear FE models to predict the failure pattern in large compression was evaluated for three boundary conditions: healthy and degenerated intervertebral discs and embedded endplates. Bone compaction and fracture patterns were predicted using the local volume change as an indicator and the best correspondence was obtained for the healthy intervertebral discs. These preliminary results show that nonlinear finite element models enable prediction of bone localization and compaction. To the best of our knowledge, this is the first study to predict the collapse of osteoporotic vertebral bodies up to large compression using realistic loading via the intervertebral discs.

Keywords: finite element analysis, spine segment, large deformations, vertebral fracture, boundary conditions, disc degeneration

1. Introduction

Vertebral compression fractures are associated with increased risk of subsequent fractures, pain, decreased quality of life, and mortality [1,2] and the risk of such fractures increases with age [3]. Dual energy x-ray absorptiometry (DXA) is currently used to estimate fracture risk clinically; however, it cannot accurately identify individuals who will suffer a fracture

[4] and does not account for three-dimensional geometry or local changes in bone density and orientation. Patient-specific nonlinear finite element models based on quantitative computed tomography (QCT) are able to predict vertebral strength more accurately than DXA [5] and models based on micro-computed tomography are being increasingly used in studies of vertebral strength and failure [6-10].

Attempts have been made to predict failure locations resulting from axial compression through patterns of strain [11,12], damage [13,14], and failed tissue [15]. Most of these finite element models, however, have been validated against experiments where the vertebral endplates were either embedded in a stiff material [16], removed [17], or fixed to rubber discs [18]. These methods eliminate the need to model the complex material behaviour of the intervertebral disc as well as ambiguity in material properties due to unknown levels of disc degeneration. However, these boundary conditions have a significant effect on the prediction of vertebral strength and failure patterns [19-22]. Additionally, failure of vertebrae loaded via healthy intervertebral discs is often initiated in the endplates [23,24] and the constraint imposed by the unrealistically stiff experimental boundary conditions, such as polymethylmethacrylate (PMMA) embedding, prevents deformation of the endplates, and thus, simulation of this common type of vertebral failure. Moreover, models that have simulated loading via the intervertebral disc have used simple linear elastic material models for the disc without direct experimental validation [25-27].

The majority of finite element models used to study vertebral strength and failure have been implemented only for small strains [17,18,25]. However, *in vivo*, vertebral fractures often involve significant loss of height [28,29]. While simulation up to, or just beyond, initial yield provides valuable information about initial failure location, it offers little insight into subsequent areas of failure or the evolution of damage that results in bone compaction at higher compressive strains. Such information may be beneficial in understanding mechanisms of fracture and vertebral body collapse. In a recent study [30], a combined experimental and computational analysis of the collapse of single vertebral bodies embedded in PMMA under large deformation was reported. Accordingly, the aim of this study is to extend the previous results to the collapse of vertebral bodies loaded via the intervertebral discs.

Specimen-specific nonlinear finite element models were developed for two spine segments tested experimentally in stepwise loading beyond 30% vertebral compression. The ability of the two models to predict the experimental failure pattern was evaluated using both healthy and degenerated disc conditions, as well as embedding of the vertebral endplates.

2. Material and Methods

2.1 Experiment

2.1.1 Sample Preparation

Two spine segments were obtained from a single human cadaver spine donated to the Centre of Anatomy and Cell Biology of the Medical University of Vienna with the signed informed consent requested by the local ethics commission. Each segment consisted of one full vertebral body between two intervertebral discs and two half-vertebral bodies (Specimen 1: T9-T11, Specimen 2: T11-L1). The cadaver spine was stored at -20°C prior to sample dissection and hydration was maintained using 0.9% saline solution during preparation. Spine segments were obtained by cutting vertebral bodies transversely, cleaning surrounding soft tissue, and isolating from their posterior elements. For each segment, the inferior and superior half-vertebral bodies were embedded in PMMA such that approximately 5 mm of bone remained out of the PMMA block in the half-vertebrae.

2.1.2 Mechanical Testing

The spine segments were loaded in a stepwise manner with a device used in a previous study [30] designed to apply a compressive load inside a high-resolution peripheral computed tomography (HR-pQCT) machine. The PMMA surfaces of the segment were glued to the loading platens of the device and the radiolucent chamber was filled with 0.9% saline solution. A fine-thread screw connected to a thrust bearing was used to manually control axial displacement without applying any torque. During the mechanical testing, radial pin holes allowed approximate tracking of applied displacement and a load cell contained in the device captured the resulting force. The registered HR-pQCT images enabled the exact measurement of the applied axial displacements corresponding to the varying number of voxels in the cranio-caudal direction at each loading step. Due to the stepwise nature of the experiments and the sharp drop of force after failure, it was not possible to accurately capture the force-displacement curves. Instead, the focus was prediction of failure zones as this is of greater importance in large strain analysis of bone compaction.

To image the initial configuration of the segments, a preload was applied to fix the specimen in place and minimize time spent in the toe region and the device was imaged using a HR-pQCT system (XtremeCT, Scanco Medical AG, Brüttisellen, Switzerland) at a resolution of 82μm. For all subsequent steps, displacement was applied using the loading screw, the specimen was allowed to relax for 25 minutes, and then the device was imaged, resulting in a total relaxation time of 50 minutes. This process was repeated until approximately 30% deformation was achieved in the central vertebral body, with applied displacement being increased following loading step 3 and 6 while relaxation time was kept constant. The displacement applied to the spine segments at each loading step as measured on the HR-pQCT images is given in Table 1. The increasing rate of applied compression allowed completion of each stepwise loading experiment within 12 hours.

2.2 Finite Element Model

2.2.1 Mesh Generation

HR-pQCT images obtained of the initial configuration were used to create finite element meshes consisting of quadratic tetrahedral elements for the vertebral bodies of the spine segments following an automated meshing procedure [31,32] in Medtool (www.dr-pahr.at). An analysis of mesh sensitivity using this meshing procedure and material model was performed previously [14,33]. To create meshes for the intervertebral discs, the space between vertebral bodies was manually segmented from the HR-pQCT images in ITK-SNAP [34] and converted into an analytic surface in SolidWorks (Dassault Systèmes, Vélizy-Villacoublay, France). This surface was then meshed with linear hexahedral elements in CUBIT (Sandia National Laboratories, Albuquerque, New Mexico) and elements were sets created for the nucleus pulposus and annulus fibrosus such that the nucleus represented approximately 43% of the total intervertebral disc volume [19,35]. Finally, to establish an interface between the discs and the vertebral endplates, the corresponding surfaces were tied. The resulting meshes of the spine segments (Figure 1A) comprised 29630 and 44808 elements for Specimens 1 and 2, respectively.

For the embedded boundary condition case, two PMMA blocks were extruded from the endplates of the centre vertebral body mesh using quadratic tetrahedral elements, as shown in Figure 1B. Small-sliding contact was then implemented between PMMA and bone surfaces not in contact in the initial configuration with a negligible friction coefficient ($\mu = 0.01$) only to prevent penetration of the PMMA by cortical elements at large deformations.

2.2.2 Material Models

To account for the heterogeneity and anisotropy of bone, the bone volume over total volume (BV/TV) and fabric tensor were extracted from the HR-pQCT images of the initial configuration and mapped to the corresponding integration points of each element [32]. A nonlocal implicit gradient-enhanced damage-plastic model implemented to model the constitutive behaviour of bone for the spine segments was then used to interpret the elements' BV/TV and trabecular anisotropy as elastic and strength properties. The material constants for strength and elasticity were determined from uni- and multi-axial tests on human trabecular samples [36]. Details regarding the implementation of this model are available elsewhere [30,33].

For the "healthy" intervertebral discs, the annulus fibrosus was modelled as a reduced polynomial hyper-elastic material with $C_{10} = 0.025$ MPa, $C_{20} = 0.625$ MPa, and $D_1 = 1.224$ MPa^{-1} and the nucleus pulposus as a Neo-Hookean hyper-elastic material with $C_{10} = 0.04$ MPa and $D_1 = 0.096$ MPa^{-1}. These coefficients were obtained by scaling reported values [37] by 0.25 to account for the relaxation between loading steps and the substantially lower strain rate in our experiments such that simulated and experimental ultimate loads agreed for both specimens. A trial simulation found little effect of annulus fibres in axial compression; therefore, for simplicity, annular fibres were not accounted for. Since the degenerative process generally begins with the nucleus losing water content and becoming more fibrous, moderate "degeneration" of the disc was approximated by using the material model of the annulus for the nucleus as well [25,38]. Finally, PMMA was modelled as a linear elastic material with E = 3000 MPa and ν = 0.3 [39].

2.2.3 Simulation

All simulations were performed in Abaqus 6.11 (Dassault Systèmes, Vélizy-Villacoublay, France). For the spine segments, peripheral nodes on the lower half of the inferior half-vertebra were fixed and displacement was applied in the axial direction to nodes on the upper half of the superior half-vertebra (Figure 1). The applied displacement corresponded to the total experimental displacement applied to the spine segment measured in the HR-pQCT images. For the embedded endplates model, displacement equivalent to the average change in height of the centre vertebral body in each experiment was applied to the superior nodes of the superior PMMA block while the inferior block was constrained.

The total resultant force on the specimen was calculated and the trace of the finite strain tensor, tr(**E**), was computed for each element. The Eulerian strain **E** (not to be confused with the Green-Lagrangian strain measure) was defined as the approximation of the integral of the rate of deformation tensor ($\int \mathbf{D} dt$) [33]. It can be demonstrated that its trace is equivalent to the logarithm of the change of volume ($\ln(\det(\mathbf{F}))$) [30]. Therefore, negative values of tr(**E**) represent compression of material and indicate bone compaction while positive values represent expansion of material as a result of applied tension, which may lead to fracture. Therefore, tr(**E**) was compared with bone compaction in the experiments, observable in the HR-pQCT images.

3. Results

In the mechanical testing, after early collapse of the superior endplate (Magerl classification A1.1) [40], a superior wedge fracture (A1.2.1) occurred in Specimen 1 (Figure 2) and an average deformation of approximately 30% was achieved after 10 loading steps. The superior endplate of the centre vertebra was damaged by a shallow crack running in the coronal plane across the vertebra. In Specimen 2, an average deformation of approximately 35% was achieved after 11 loading steps. The posterior wall and both endplates were fractured and the right-posterior section was nearly separated from the main vertebral body (Figure 3, Figure 4). A comparison between experimental and simulated ultimate loads is provided in Table 2.

On average, the simulations required 14 hours for the full spine segments and 4 hours for the embedded vertebral body on four 3 GHz processors of a standard PC with 24 GB RAM.

A comparison of the measure of local volume change, tr(**E**), between simulated boundary conditions and with the experimental images is shown in Figures 2 and 3 for selected loading steps. Bone compaction begins later in the degenerated disc case than the other two cases and the degenerated intervertebral discs are compressed more than the healthy ones. Additionally, the endplates undergo greater deformation in the models that include the discs than the embedded vertebral body.

The correspondence between positive changes of volume (tr(**E**) > 0) and fracture locations is shown in Figure 4. The continuum model used does not allow for fracturing of material; however, elements that experienced tension and have increased in volume, provide an indication of fracture locations as tension causes brittle fracture in bone [14].

4. Discussion

Nonlinear finite element models offer an attractive option for patient-specific prediction of vertebral failure patterns. Currently, experimentally validated models do not include physiologic boundary conditions for vertebral bodies and are rarely used in large compression. Therefore, the aim of this study was to demonstrate the ability of a nonlinear finite element model of a spine segment to predict regions of bone compaction and failure and examine the effect of boundary conditions using stepwise loading experiments.

There was good agreement between the failure pattern predicted by the model and the visible bone compaction in the HR-pQCT images. In Specimen 1, the model correctly predicted localization beneath the superior endplate and the buckling in the superior anterior cortex. The shear band that occurred in Specimen 2 was also predicted, although with a slight posterior shift, as well as the two localized areas in the final loading step. While the model was successful in general, there were some discrepancies, including the inability to predict the small buckling in the inferior anterior cortex in Specimen 1 and the slight posterior shift of the localized band in Specimen 2. These can be partly attributed to the imprecision in the meshing procedure, especially for the outer rim of the endplates, since the accuracy of the outer geometry is limited by the element size. Furthermore, the cortex was modelled as slightly thicker than in reality by including a small amount of trabecular bone to attenuate the bone volume fraction in the cortex, thus enabling the use of the same material model for trabecular and cortical bone.

While the bone compaction predicted using different boundary conditions generally occurs in the same location, some differences were observed. The effect of the nucleus in the load transfer to the vertebra in the healthy disc model is highlighted by the inward bulging of the endplates occurring in both specimens, especially the early endplate disruption in Specimen 1. This is not seen in the degenerated case, which may be an indication of a shift in load bearing from the nucleus to the annulus, as has been observed previously with degeneration [41,42]. This study also agreed with results obtained *in silico* indicating that failure patterns resulting from loading via the intervertebral disc and PMMA are not equivalent [19,42] under large compression. In the embedded case, the rigid constraint imposed by the PMMA prevents deformation of the endplates as well as shearing of material in the transverse plane. Because of this, types of fractures observed *in vivo*, such as biconcave or wedge fractures [29], seen to some extent in these experiments, cannot be replicated with rigid boundary conditions. The results for the degenerated discs lie somewhere between those of the healthy disc and PMMA cases, suggesting that while embedded models do not accurately replicate physiologic loading, they more closely represent the boundary conditions imposed by a degenerated disc than a healthy one.

Although the bone model presented here is unable to simulate fractures, it was capable of predicting fracture locations by highlighting zones subjected to volumetric tensile strain. A large fracture of material did not occur in Specimen 1; however, in Specimen 2, fracture locations were correctly represented by positive changes in volume. While fracture locations are best represented by the healthy disc model, the degenerated disc model was able to capture the majority of fractures as well. It is noteworthy that the embedded endplates model did not predict any of the fractures as stretching of the endplates is prevented by the PMMA.

An important limitation of this study is the model used for the disc. Although the hyper-elastic material model that was implemented is more representative of true intervertebral disc behaviour than the linear elastic models that have been used previously [25,27], it is still fairly simplistic and does not capture the complex, time-dependent, anisotropic, and heterogeneous nature of the disc, nor the ability of the nucleus to flow outside of the annulus or into the endplates. While sophisticated poro-elastic models do exist, these have so far only been used to investigate behaviour of the disc itself and not its impact on load transfer [43-46]. Identification of the disc's material properties and morphology requires accurate MRI and experimental data [22]. Although the radial expansion of the nucleus under compression generates hoop stresses in the annular fibres [47], the compressive load is essentially carried by the matrix [48]. Our trials indeed revealed a lack of impact of the fibres, which were not included in the simulations. Also, it can be seen in Figures 2 and 3 that the discs deform more in the experiments than in the simulations. Such large deformations are difficult to attain in simulations without encountering excessive element distortion and consequent numerical instabilities. The results obtained here could potentially be further improved through implementation of a more complex and better representative intervertebral disc model. Additionally, the ability to quantify disc degeneration and local material properties through methods such as magnetic resonance imaging (MRI) could provide valuable information to better replicate the true boundary conditions [49].

Another limitation was the inclusion of only two samples. This was a result of the large amount of time and manual work required to complete the stepwise loading experiments and generate the FE meshes. Improved meshing algorithms should enable larger studies in the future. The small sample size, however, did allow a detailed qualitative analysis of trabecular bone collapse, endplate deflection, cortex buckling, and fracture zone detection at large compressive strains.

Despite these limitations, the potential for a nonlocal damage-plastic model for bone used for a spine segment including intervertebral discs to accurately predict failure patterns in large compression has been demonstrated in a detailed analysis of two samples tested experimentally in stepwise loading. The model was able to correctly predict areas of bone compaction and fracture using the local volume change as an indicator. Furthermore, it was confirmed that models with endplate embedding in PMMA are not able to replicate fractures that occur *in vivo* as a result of loading through the intervertebral disc.

Acknowledgements

This project was supported by the European Community under Grant Agreement PITN-GA-2009-238690-SPINEFX.

References

[1] Lindsay R, Silverman SL, Cooper C, Hanley DA, Barton I, Broy SB, et al. Risk of new vertebral fracture in the year following a fracture. JAMA 2001; 285: 320–3.

[2] Kanis JA, Oden A, Johnell O, De Laet C, Jonsson B. Excess mortality after hospitalisation for vertebral fracture. Osteoporos Int 2004; 15(2): 108–12.

[3] O'Neill TW, Felsenberg D, Varlow J, Cooper C, Kanis JA, Silman AJ. The prevalence of vertebral deformity in european men and women: the European Vertebral Osteoporosis Study. J Bone Miner Res 1996; 11(7): 1010–8.

[4] Marshall D, Johnell O, Wedel H. Meta-analysis of how well measures of bone mineral density predict occurrence of osteoporotic fractures. BMJ 1996; 312: 1254–9.

[5] Dall'Ara E, Pahr DH, Varga P, Kainberger F, Zysset PK. QCT-based finite element models predict human vertebral strength in vitro significantly better than simulated DEXA. Osteoporos Int 2012; 23(2): 563–72.

[6] Chevalier Y, Quek E, Borah B, Gross G, Stewart J, Lang T, et al. Biomechanical effects of teriparatide in women with osteoporosis treated previously with alendronate and risedronate: results from quantitative computed tomography-based finite element analysis of the vertebral body. Bone 2010; 46(1): 41–8.

[7] Fields AJ, Lee GL, Liu XS, Jekir MG, Guo XE, Keaveny TM. Influence of vertical trabeculae on the compressive strength of the human vertebra. J Bone Miner Res 2011; 26(2): 263–9.

[8] Graeff C, Chevalier Y, Charlebois M, Varga P, Pahr D, Nickelsen TN, et al. Improvements in vertebral body strength under teriparatide treatment assessed in vivo by finite element analysis: results from the EUROFORS study. J Bone Miner Res 2009; 24(10): 1672–80.

[9] Matsumoto T, Ohnishi I, Bessho M, Imai K, Ohashi S, Nakamura K. Prediction of vertebral strength under loading conditions occurring in activities of daily living using a computed tomography-based nonlinear finite element method. Spine 2009; 34(14): 1464–9.

[10] Melton III LJ, Riggs BL, Keaveny TM, Achenbach SJ, Hoffmann PF, Camp JJ, et al. Structural determinants of vertebral fracture risk. J Bone Miner Res 2007; 22(12): 1885–92.

[11] Imai K, Ohnishi I, Bessho M, Nakamura K. Nonlinear finite model predicts vertebral bone strength and fracture site. Spine 2006; 31(16): 1789-94.

[12] Silva MJ, Keaveny TM, Hayes WC. Computed tomography-based finite element analysis predicts failure loads and fracture patterns for vertebral sections. J Orthop Res 1998; 16(3): 300–8.

[13] Chevalier Y, Charlebois M, Pahr D, Varga P, Heini P, Schneider E, et al. A patient-specific finite element methodology to predict damage accumulation in vertebral bodies under axial compression, sagittal flexion and combined loads. Comput Methods Biomech Biomed Engin 2008; 11(5): 477–87.

[14] Hosseini HS, Pahr DH, Zysset PK. Modeling and experimental validation of trabecular bone damage, softening and densification under large compressive strains. J Mech Behav Biomed Mater 2012; 15: 93–102.

[15] Fields AJ, Nawathe S, Eswaran SK, Jekir MG, Adams MF, Papadopoulos P, et al. Vertebral fragility and structural redundancy. J Bone Miner Res 2012; 27(10): 2152–8.

[16] Christiansen BA, Kopperdahl DL, Kiel DP, Keaveny TM, Bouxsein ML. Mechanical contributions of the cortical and trabecular compartments contribute to differences in age-related changes in vertebral body strength in men and women assessed by QCT-based finite element analysis. J Bone Miner Res 2011; 26(5): 974–83.

[17] Dall'Ara E, Schmidt R, Pahr D, Varga P, Chevalier Y, Patsch J, et al. A nonlinear finite element model validation study based on a novel experimental technique for inducing anterior wedge-shape fractures in human vertebral bodies in vitro. J Biomech 2010; 43(12): 2374–80.

[18] Mirzaei M, Zeinali A, Razmjoo A, Nazemi M. On prediction of the strength levels and failure patterns of human vertebrae using quantitative computed tomography (QCT)-based finite element method. J Biomech 2009; 42(11): 1584–91.

[19] Maquer G, Schwiedrzik J, Zysset PK. Embedding of human vertebral bodies leads to higher ultimate load and altered damage localisation under axial compression. Comput Methods Biomech Biomed Engin 2012; 17(12): 1311–22.

[20] Yerby SA, Bay BK, Toh E, McLain RF, Drews MJ. The effect of boundary conditions on experimentally measured trabecular strain in the thoracic spine. J Biomech 1998; 31(10): 891–7.

[21] Lu Y, Maquer G, Museyko O, Püschel K, Engelke K, Zysset P, et al. Finite element analyses of human vertebral bodies embedded in polymethylmethalcrylate or loaded via the hyperelastic intervertebral disc models provide equivalent predictions of experimental strength. J Biomech 2014; 47: 2512–6.

[22] Maquer G, Schwiedrzik J, Huber G, Morlock MM, Zysset PK. Compressive strength of elderly vertebrae is reduced by disc degeneration and additional flexion. J Mech Behav Biomed Mater 2014; 42: 54-66.

[23] McBroom RJ, Hayes WC, Edwards WT, Goldberg RP, White III AA. Prediction of vertebral body compressive fracture using quantitative computed tomography. J Bone Joint Surg Am 1985; 67-A(8): 1206–14.

[24] Shirado O, Kaneda K, Tadano S, Ishikawa H, McAfee PC, Warden KE. Influence of disc degeneration on mechanism of thoracolumbar burst fractures. Spine 1992; 17(3): 286–92.

[25] Eswaran SK, Gupta A, Keaveny TM. Locations of bone tissue at high risk of initial failure during compressive loading of the human vertebral body. Bone 2007; 41(4): 733–739.

[26] Fields AJ, Lee GL, Keaveny TM. Mechanisms of initial endplate failure in the human vertebral body. J Biomech 2010; 43(16): 3126–31.

[27] Nekkanty S, Yerramshetty J, Kim D-G, Zauel R, Johnson E, Cody DD, et al. Stiffness of the endplate boundary layer and endplate surface topography are associated with brittleness of human whole vertebral bodies. Bone 2010; 47(4): 783–89.

[28] Eastell R, Cedel SL, Wahner HW, Riggs BL, Melton III LJ. Classification of vertebral fractures. J Bone Miner Res 1991; 6(3): 207–15.

[29] Genant HK, Wu CY, Van Kuijk C, Nevitt MC. Vertebral fracture assessment using a semiquantitative technique. J Bone Miner Res 1993; 8(9): 1137–48.

[30] Hosseini HS, Clouthier AL, Zysset PK. Experimental validation of finite element analysis of human vertebral collapse under large compressive strains. J Biomech Eng 2014; 136(4): 041006.

[31] Pahr DH, Zysset PK. A comparison of enhanced continuum FE with micro FE models of human vertebral bodies. J Biomech 2009; 42(4): 455–62.

[32] Pahr DH, Zysset PK. From high-resolution CT data to finite element models: development of an integrated modular framework. Comput Methods Biomech Biomed Engin 2009; 12(1): 45–57.

[33] Hosseini HS. Constitutive modeling of trabecular bone in large strain compression [dissertation]. Bern: University of Bern; 2013.

[34] Yushkevich PA, Piven J, Cody H, Hazlett C, Smith RG, Ho S, et al. User-guided 3D active contour segmentation of anatomical structures: significantly improved efficiency and reliability. Neuroimage 2006; 31(3): 1116-28.

[35] White III A, Panjabi M. Clinical Biomechanics of the Spine. Philadelphia: J.B. Lippincott; 1990.

[36] Ricón-Kohli L, Zyssett PK. Multi-axial mechanical properties of human trabecular bone. Biomech Model Mechan 2009; 8(3): 195-208.

[37] Moramarco V, Pérez del Palomar A, Pappalettere C, Doblaré M. An accurate validation of a computational model of a human lumbosacral segment. J Biomech 2010; 43(2): 334–42.

[38] Polikeit A, Nolte LP, Ferguson SJ. Simulated influence of osteoporosis and disc degeneration on the load transfer in a lumbar functional spinal unit. J Biomech 2004;. 37(7): 1061–9.

[39] Lewis G. Properties of acrylic bone cement: state of the art review. J Biomed Mater Res A 1997; 38(2): 155-82.

[40] Magerl F, Aebi M, Gertzbein SD, Harms J, Nazarian S. A comprehensive classification of throacic and lumbar injuries. Eur Spine J 1994; 3: 184-201.

[41] Adams MA, Dolan P. Intervertebral disc degeneration: evidence for two distinct phenotypes. J Anat 2012; 221: 497-506.

[42] Homminga J, Aquarius R, Bulsink VE, Jansen CTJ, Verdonschot N. Can vertebral density changes be explained by intervertebral disc degeneration? Med Eng Phys 2012; 34(4): 453-8.

[43] Erdem I, Truumees E, van der Meulen MCH. Simulation of the behaviour of the L1 vertebra for different material properties and loading conditions. Comput Methods Biomech Biomed Engin 2013; 16(7): 736-746.

[44] Galbusera F, Schmidt H, Noailly J, Malandrino A, Lacroix D, Wilke H-J, et al. Comparison of four methods to simulate swelling in poroelastic finite element models of intervertebral discs. J Mech Behav Biomed Mater 2011; 4(7): 1234–41.

[45] Pérez del Palomar A, Calvo B, Doblaré M. An accurate finite element model of the cervical spine under quasi-static loading. J Biomech 2008; 41(3): 523–31.

[46] Rohlmann A, Zander T, Schmidt H, Wilke H-J, Bergmann G. Analysis of the influence of disc degeneration on the mechanical behaviour of a lumbar motion segment using the finite element method. J Biomech 2006; 39(13): 2484–90.

[47] Cortes DH, Elliott DM. Extra-fibrillar matrix mechanics of annulus fibrosus in tension and compression. Biomech Model Mechanobiol. 2012; 11(6): 781–90.

[48] Adams MA, Roughley PJ. What is intervertebral disc degeneration, and what causes it? Spine 2006; 31(18): 2151–61.

[49] Maquer G, Brandejsky V, Benneker LM, Watanabe A, Vermathen P, Zysset PK. Human intervertebral disc stiffness correlates better with the Otsu threshold

computed from axial T2 map of its posterior annulus fibrosus than with clinical classifications. Med Eng Phys 2014; 36 (2): 219–25.

Figure Captions

Figure 1: Finite Element Meshes: Finite element meshes used for Specimen 2. A) Mesh for the whole spine segment, including intervertebral discs. B) Mesh with PMMA embedding of centre vertebra endplates. Displacements and constraints were applied as shown.

Figure 2: Specimen 1 Experimental and FE Results: Midplane images of selected steps from experimental and finite element analysis for Specimen 1. Areas where bone is compacting in the HR-pQCT images are indicated with arrows and correspond to **negative** values of the trace of the strain tensor, tr(**E**), shown in **red**.

Figure 3: Specimen 2 Experimental and FE Results: Midplane images of selected steps from experimental and finite element analysis for Specimen 2. Areas where bone is compacting in the HR-pQCT images are indicated with arrows and correspond to **negative** values of the trace of the strain tensor, tr(**E**), shown in **red**. The fracture in the centre vertebra occurred following loading step 8 and is displayed in detail in Figure 4.

Figure 4: Fracture Prediction: A and C show two three dimensional views of the segmented experimental image showing the fracture that occurred in Specimen 2. B and D show the corresponding simulation results for the healthy disc model with **positive** values of the trace of the strain tensor displayed in **red**.

Table Captions

Table 1: Applied Displacement: The displacement applied by the loading screw to the spine segments, measured from the HR-pQCT images. The applied displacement was increased after load steps 3 and 6.

Table 2: Ultimate Load: The ultimate loads for the specimens in the experiments and three simulations.

Figure 1

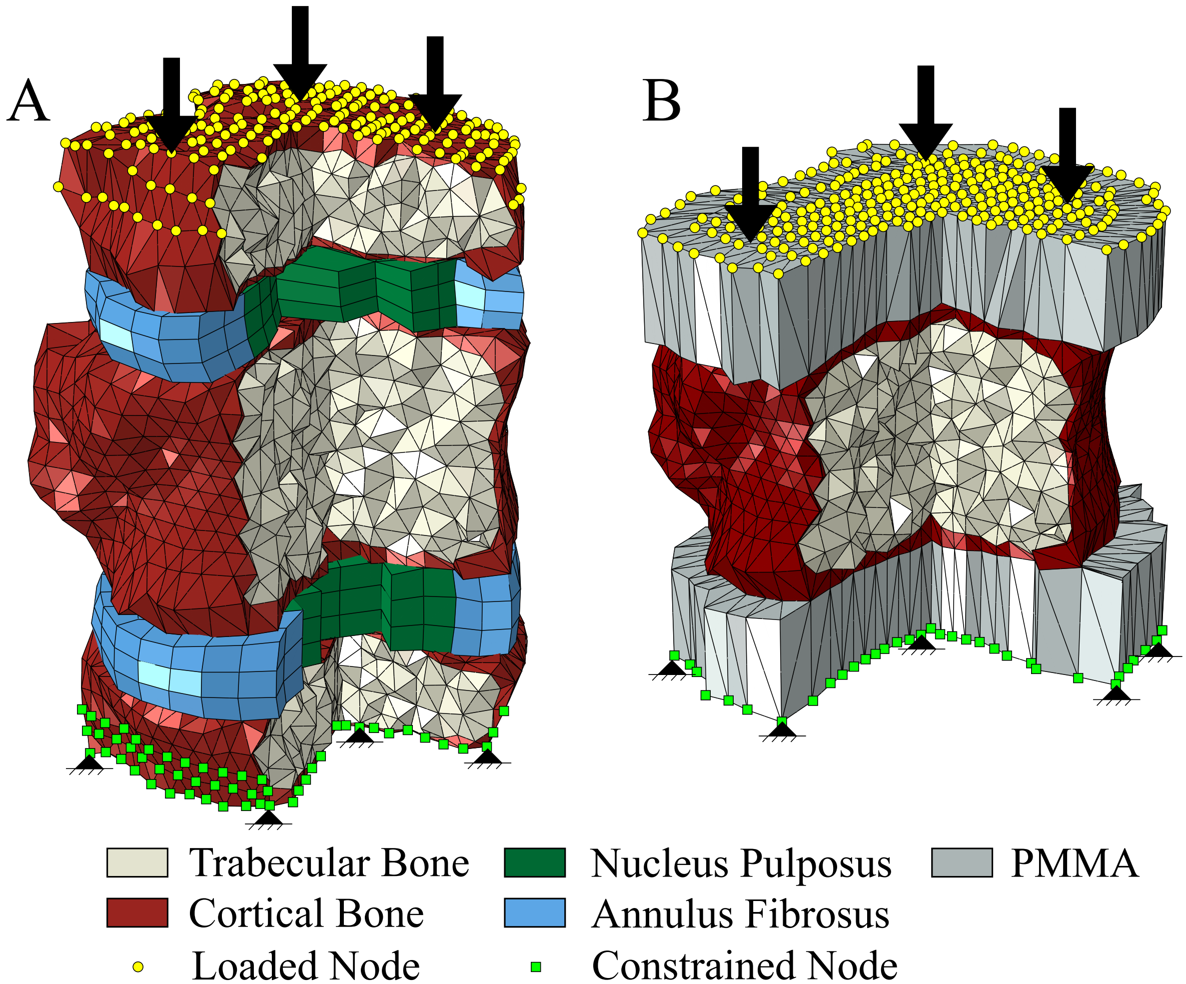
A
B
Trabecular Bone
Cortical Bone
Loaded Node
Nucleus Pulposus
Annulus Fibrosus
Constrained Node
PMMA

Figure 2

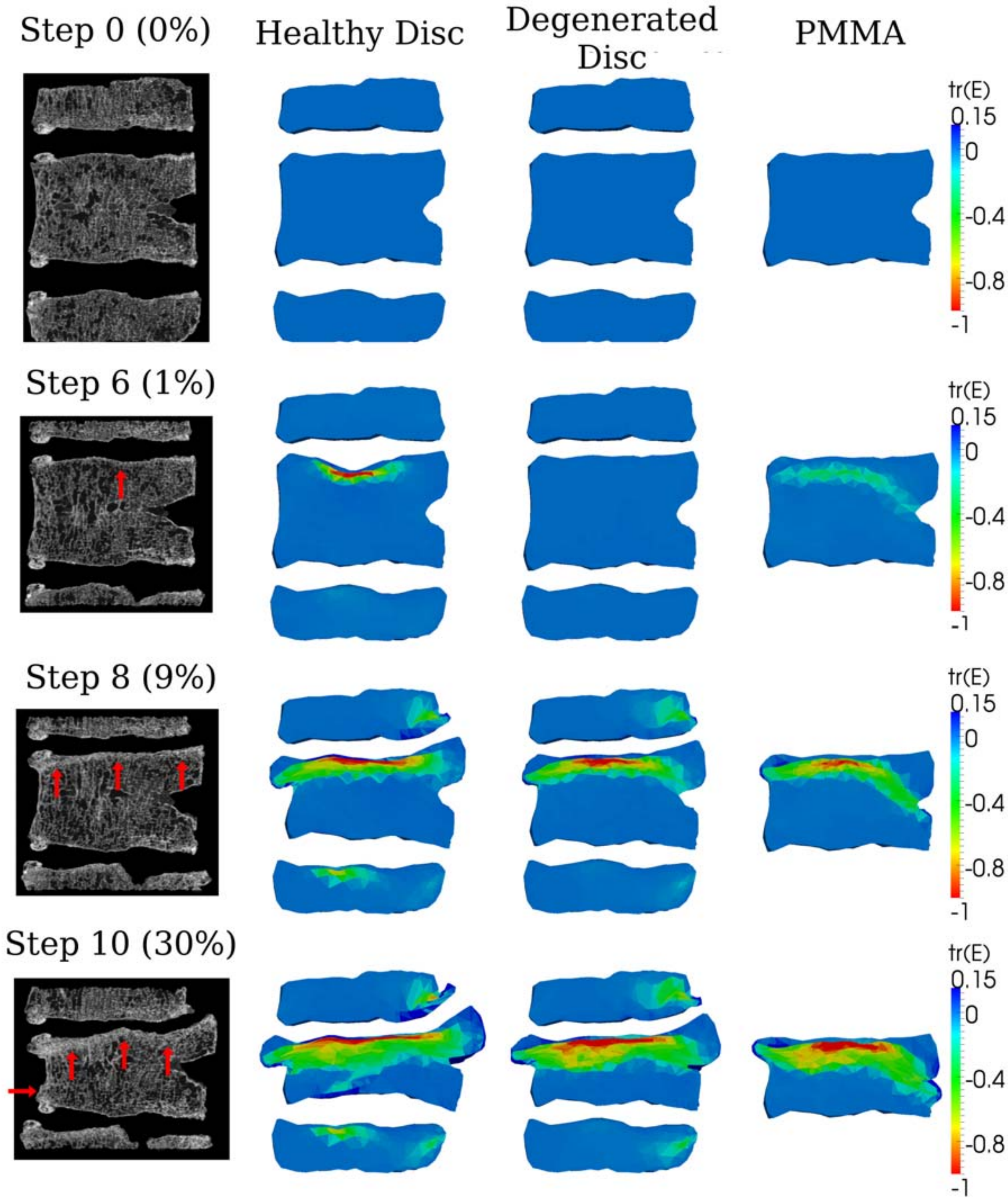
Step 0 (0%)
Healthy Disc
Degenerated Disc
PMMA
tr(E)
0.15
0
-0.4
-0.8
-1
Step 6 (1%)
Step 8 (9%)
Step 10 (30%)

Figure 3

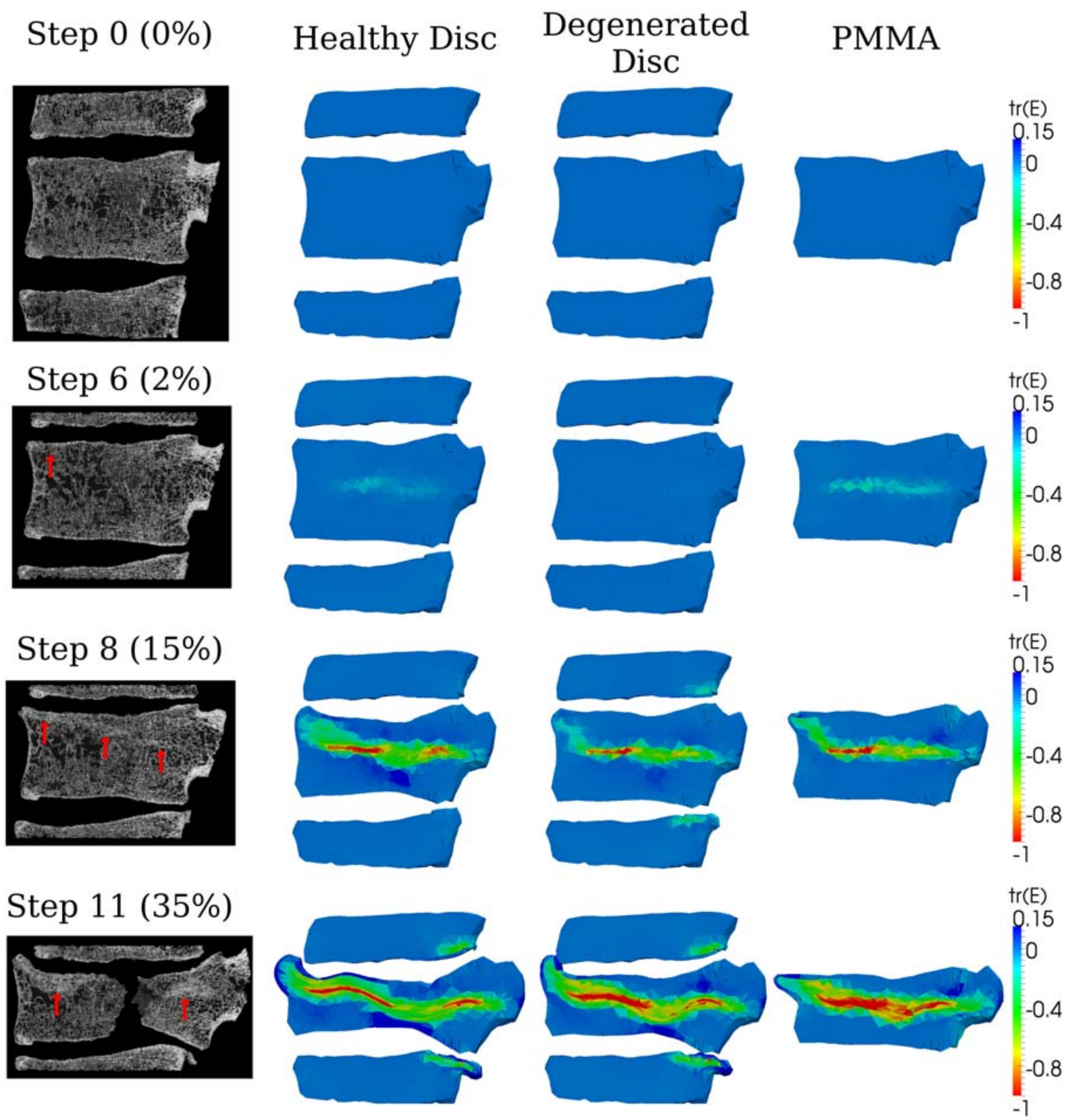
Step 0 (0%)
Healthy Disc
Degenerated Disc
PMMA
Step 6 (2%)
Step 8 (15%)
Step 11 (35%)
tr(E)
0.15
0
-0.4
-0.8
-1

Figure 4

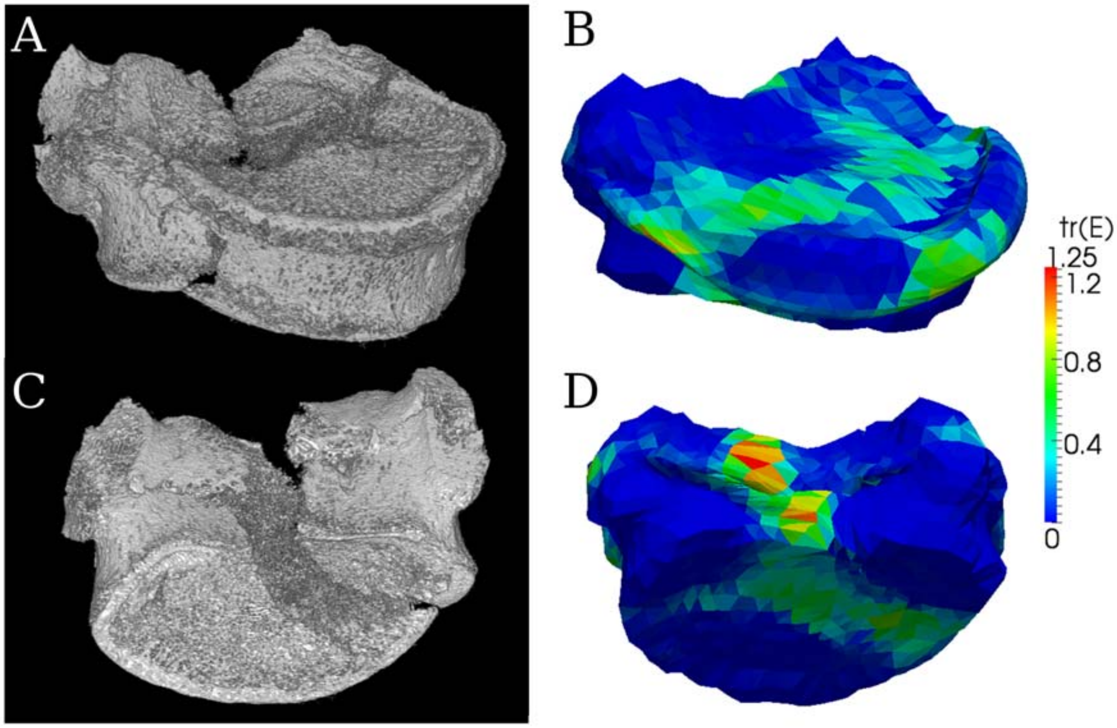

Table 1

Load Step	**Applied Displacement (mm)**	
	Specimen 1	*Specimen 2*
1	0.16	0.33
2	0.49	0.66
3	0.90	1.07
4	1.80	1.97
5	2.79	2.87
6	3.85	3.94
7	6.15	6.07
8	8.36	8.20
9	10.66	10.91
10	13.20	13.45
11		15.99

Table 2

	Ultimate Load (N)	
	Specimen 1	*Specimen 2*
Experiment	3381	3173
Healthy Disc	2626	2801
Degenerated Disc	3137	3125
PMMA	3615	3599